Originally published 20 August 2010; corrected 7 October 2010

www.sciencemag.org/cgi/content/full/329/5994/940/DC1

Supporting Online Material for

Drought-Induced Reduction in Global Terrestrial Net Primary Production from 2000 Through 2009

Maosheng Zhao* and Steven W. Running

*To whom correspondence should be addressed. E-mail: zhao@ntsg.umt.edu

Published 20 August 2010, *Science* **329**, 940 (2010)
DOI: 10.1126/science.1192666

This PDF file includes:

SOM Text
Figs. S1 to S14
Tables S1 to S6
References and Notes

Correction: In SOM Text S11, the authors mistakenly referred to a positive correlation as a negative correlation. The error has been corrected in this version.

Contents

Text S1) MODIS GPP/NPP algorithm

We used the MODIS GPP/NPP (MOD17) algorithm (S*1*, S*2*) to calculate global 1-km MODIS NPP from 2000 through 2009. The algorithm calculates daily GPP as

$$GPP = \varepsilon_{\max} * 0.45 * SWrad * FPAR * fVPD * fT_{\min} \tag{1}$$

where $\varepsilon_{\max}$ is the maximum light use efficiency; $SWrad$ is short-wave downward solar radiation, of which 45% is Photosynthetically Active Radiation (PAR); $FPAR$ is Fraction of PAR being absorbed by the plants; $fVPD$ and $fT_{\min}$ are the reduction scalar from water stresses (high daily time Vapor Pressure Deficit, VPD) and low temperature (low daily minimum temperature $T_{\min}$), respectively.

The MODIS GPP/NPP algorithm has been modified since we generated the improved Collection 5 (C5) dataset (S*2*). We modified the autotrophic respiration calculation in the algorithm. There are two major modifications:

1) The original MODIS algorithm calculated annual growth respiration (R_g) as a function of annual maximum LAI. As a result, for a given forest biome type, R_g is almost invariable across space and time due to the saturation of MODIS annual maximum LAI for forests, which is unreasonable according to plant physiological principles (S*3*, S*4*). We have, therefore, modified it by assuming growth respiration is approximately 25% of NPP (S*3*, S*4*) for C5 MOD17. Finally, annual NPP can be computed as

$$NPP = \sum_{i=1}^{365}(GPP - R_m) - R_g = \sum_{i=1}^{365}(GPP - R_m) - 0.25 * NPP \tag{2}$$

Therefore,

$$\begin{aligned} NPP &= 0.8 * \sum_{i=1}^{365}(GPP - R_m) && \text{when } \sum_{i=1}^{365}(GPP - R_m) \geq 0 \\ NPP &= 0 && \text{when } \sum_{i=1}^{365}(GPP - R_m) < 0 \end{aligned} \tag{3}$$

where R_m is the maintenance respiration.

2) For maintenance respiration (R_m), Q_{10} theory is used (S*3*), and maintenance respiration index (MRI) is a function of daily average air temperature (T_{avg})

$$MRI = Q_{10}^{\left(\frac{T_{avg} - 20}{10}\right)} \tag{4}$$

Previously Q_{10} was assumed to be a constant value of 2.0 for leaves, fine roots and live wood. For leaves, the new algorithm adopted a temperature-acclimated Q_{10} equation proposed by Tjoelker et al. (S*5*),

$$Q_{10} = 3.22 - 0.046 * T_{avg} \quad (5)$$

Using the C5 FPAR/LAI (MOD15A2) (S*6*), and NCEP/DOE II daily reanalysis datasets (S*7*) as inputs, and an existing validated improved Collection 4.5 (S*8*, S*9*) and further improved Collection4.8 MODIS GPP/NPP (S*2*) as references, we recalibrated BPLUT for this study following the method described in S*10* (Tables S1).

We ran 1-km MODIS GPP/NPP at 1-km resolution from 2000 to 2009 with 1-km MODIS land cover, 1-km MODIS FPAR/LAI and daily NCEP/DOE II as inputs following the improved MODIS GPP/NPP procedure (S*10*). Figure S1 shows that spatial pattern of mean NPP for the past 10 years. The next section, Text S2, details how the input datasets were processed to generate NPP at 1-km.

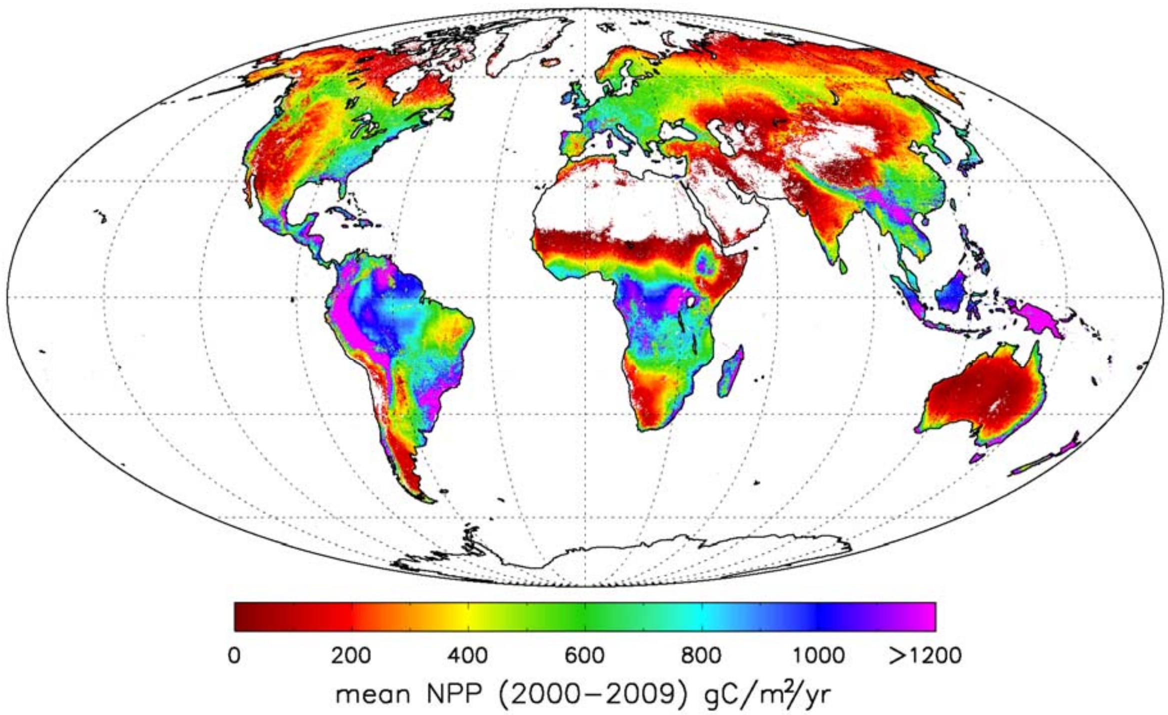

Figure S1. The spatial pattern of mean 1-km NPP for the last 10-years estimated from MODIS driven by NCEP/DOE II. The white colored areas on land are non-vegetated pixels, such as inland water body, barren and urban as defined by MODIS land cover in Figure S2.

Table S1. Biome-Property-Look-Up-Table (BPLUT) for MODIS GPP/NPP algorithm with NCEP-DOE reanalysis II and the Collection5 FPAR/LAI as inputs. The full names for the University of Maryland land cover classification system (UMD_VEG_LC) in MOD12Q1 dataset (fieldname: Land_Cover_Type_2) are, Evergreen Needleleaf Forest (ENF), Evergreen Broadleaf Forest (EBF), Deciduous Needleleaf Forest (DNF), Deciduous Broadleaf Forest (DBF), Mixed forests (MF), Closed Shrublands (CShrub), Open Shrublands (OShrub), Woody Savannas (WSavanna), Savannas (Savanna), Grassland (Grass), and Croplands (Crop).

UMD_VEG_LC	ENF	EBF	DNF	DBF	MF	CShrub	OShrub	WSavanna	Savanna	Grass	Crop
LUEmax (KgC/m^2/d/MJ)	0.000962	0.001268	0.001086	0.001165	0.001051	0.001281	0.000841	0.001239	0.001206	0.000860	0.001044
Tmin_min (C)	-8.00	-8.00	-8.00	-6.00	-7.00	-8.00	-8.00	-8.00	-8.00	-8.00	-8.00
Tmin_max (C)	8.31	9.09	10.44	9.94	9.50	8.61	8.80	11.39	11.39	12.02	12.02
VPD_min (Pa)	650.0	800.0	650.0	650.0	650.0	650.0	650.0	650.0	650.0	650.0	650.0
VPD_max (Pa)	4600.0	3100.0	2300.0	1650.0	2400.0	4700.0	4800.0	3200.0	3100.0	5300.0	4300.0
SLA (LAI/KgC)	14.1	25.9	15.5	21.8	21.5	9.0	11.5	27.4	27.1	37.5	30.4
Q_{10}*	2.0	2.0	2.0	2.0	2.0	2.0	2.0	2.0	2.0	2.0	2.0
froot_leaf_ratio	1.2	1.1	1.7	1.1	1.1	1.0	1.3	1.8	1.8	2.6	2.0
livewood_leaf_ratio	0.182	0.162	0.165	0.203	0.203	0.079	0.040	0.091	0.051	0.000	0.000
leaf_mr_base	0.00604	0.00604	0.00815	0.00778	0.00778	0.00869	0.00519	0.00869	0.00869	0.0098	0.0098
froot_mr_base	0.00519	0.00519	0.00519	0.00519	0.00519	0.00519	0.00519	0.00519	0.00519	0.00819	0.00819
livewood_mr_base	0.00397	0.00397	0.00397	0.00371	0.00371	0.00436	0.00218	0.00312	0.00100	0.00000	0.00000

*: The constant Q_{10} = 2.0 is applied to fine roots and live wood, while for leaves, a temperature acclimation Q_{10} value is used as described in Equation 5.

Text S2) Remote sensing datasets

For this study, four MODIS data products were used, including the Collection4 MODIS 1-km land cover (MOD12Q1) (S*11*), the Collection5 MODIS Climate Model Grid (CMG) 0.05 degree 8-day snow cover (MOD10C2) (S*12*), the Collection5 MODIS 1-km 8-day FPAR/LAI (MOD15A2) (S*6*), and the Collection5 MODIS 16-day 1-km NDVI/EVI (MOD13A2) (S*13*). We didn't use the Collection5 MODIS land cover because the Collection5 FPAR/LAI are being generated at NASA based on canopy structure land cover from the Collection4 MODIS land cover data instead of the Collection5.

1) MODIS land cover

For both MODIS FPAR/LAI and GPP/NPP datasets, land cover types of water body, urban and barren are treated as non-vegetated area. The 1-km UMD MODIS land cover (Figure S2) is used to map corresponding BPLUT for each 1-km pixel. Based on MODIS land cover (Figure S2), there is totally 144.68 Million km^2 land area, of which 109.03 Million km^2 (or 75%) is vegetated land.

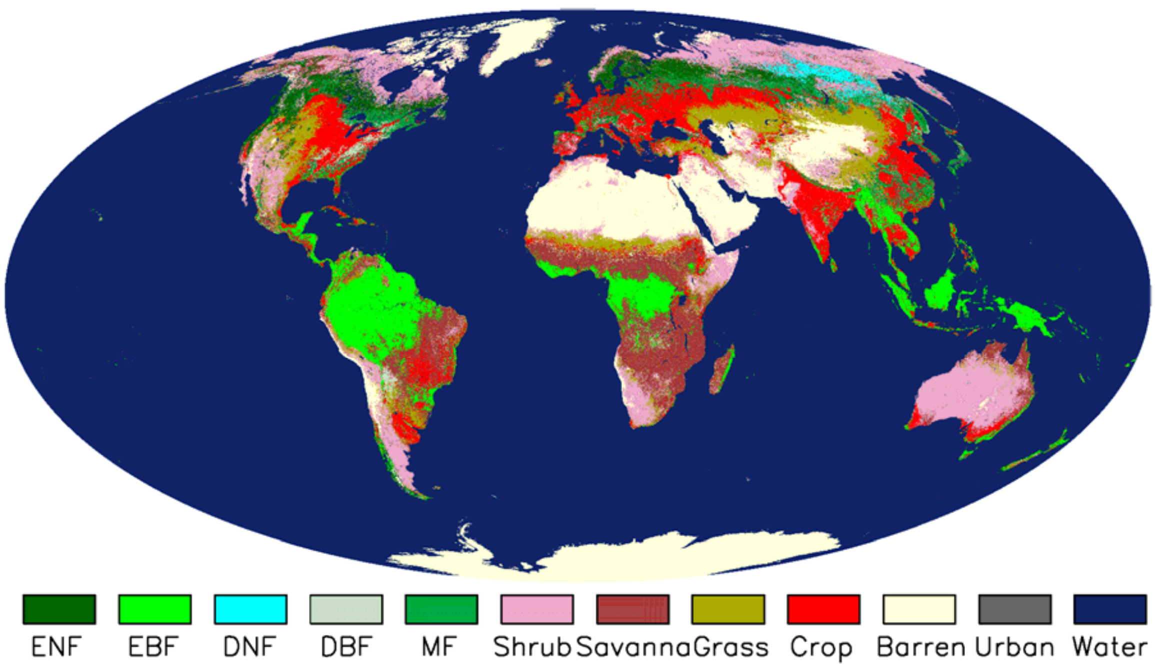

Figure S2. University of Maryland land cover classification system defined land covers from MOD12Q1 (land cover type 2 in MOD12Q1 dataset). Evergreen Needleleaf Forest (ENF), Evergreen Broadleaf Forest (EBF), Deciduous Needleleaf Forest (DNF), Deciduous Broadleaf Forest (DBF), Mixed forests (MF), Closed Shrublands (CShrub), Open Shrublands (OShrub), Woody Savannas (WSavanna), Savannas (Savanna), grassland (Grass), and Croplands (Crop). Note that in this figure, we combined CShrub and OShrub into Shrub, and WSavanna and Savannas into Savanna.

2) 1-km 8-day MODIS FPAR and LAI

The latest Collection5 1-km MODIS FPAR/LAI from 2000 through 2009 were used as vegetation dynamic inputs to run 1-km MODIS GPP/NPP for the past decade. Data gaps in 8-day FPAR/LAI caused by unfavorable atmospheric conditions, such as cloudiness and heavy aerosols, were filled based on the criteria for good quality assessment (S*10*). Prior to late February 2000, FPAR/LAI are not available, and these missing gaps were filled by averaging the corresponding 8-day reliable FPAR/LAI from 2001 to 2003, in order to calculate a complete annual MODIS GPP and NPP data set for the year 2000 (S*14*).

3) CMG MODIS snow cover data to define growing season

There are two purposes for using MODIS snow cover. First, we used it to define growing season spatially. NPP is the accumulated carbon fixed by vegetation during the growing season. Though there is plant autotrophic respiration during winter time, based on Q_{10} theory (Equation 4), its contribution to reducing NPP is relatively small due to low temperature and low living biomass (i.e., low LAI and hence low leaf biomass in dormant seasons). Air temperature is often being used to identify growing season, which suffers from both coarse resolution issues and uncertainties from reanalysis datasets. We used MODIS snow cover data to define the average growing season in order to get growing season average or total value of other meteorological variables. Secondly, we used MODIS snow cover data to show which parts of the land vegetation is mainly controlled by low temperature. Land areas with a long snow cover period generally imply a short growing season and temperature-limitation.

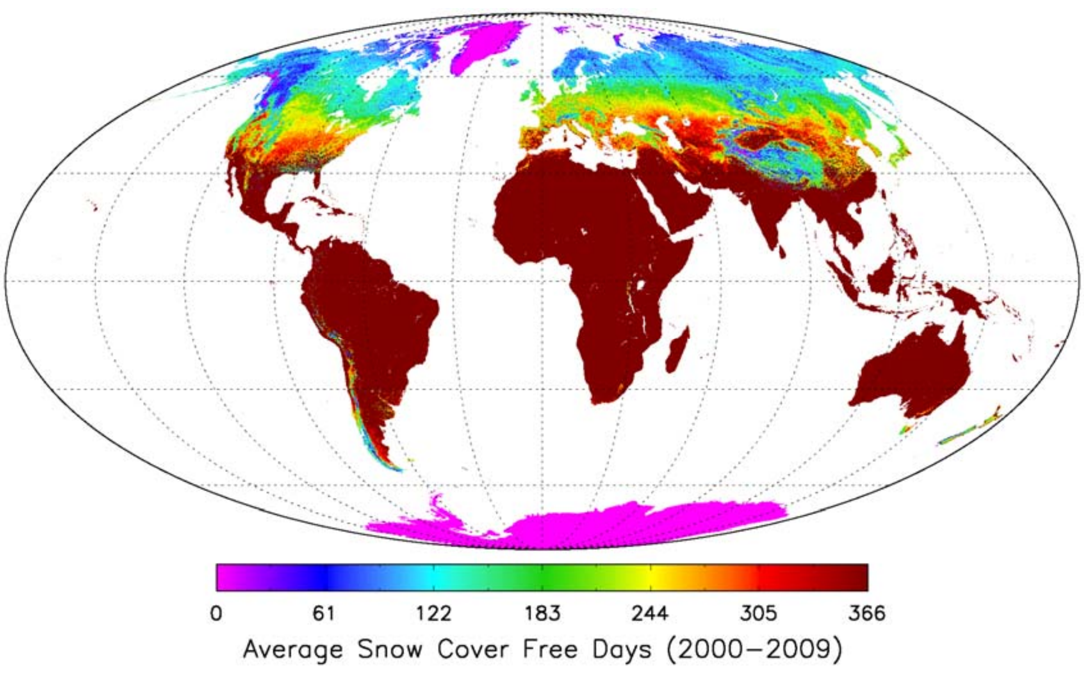

Figure S3. Average snow cover free days derived from 8-day MODIS snow cover data from 2000 through 2009. For vegetated land areas, much fewer average annual snow cover days (7.5 days) in South Hemisphere (SH) than that in North Hemisphere (NH) (125 days).

With multi-year global MOD10C2 8-day snow cover data from 2000 through 2009, we identified the first and last 8-day with no snow cover (snow cover free) for each year, and then we averaged the two periods for ten years to get the average snow cover free days for MODIS era (Figure S3). We also aggregated 8-day results into 16-day and monthly for application to other 16-day and monthly datasets. As shown in Figure S3, except for Antarctic and almost all of Greenland, where there is snow cover across the entire year and also no vegetation as defined in MOD12Q1 (Figure S2), for vegetated land areas, large parts of north hemisphere have snow cover presence within a year, while very few parts over the south hemisphere do. Though in some cases, such as deserts in Northwestern China, there is a long winter season but no snow cover, it is so dry that there is almost non-vegetation, being classified as barren (*non-vegetated*) by MODIS land cover (Figure S2).

4) 1-km 16-day MODIS NDVI

Integrated NDVI over the growing season has been traditionally used as a surrogate of NPP (S*15*). We used NDVI to verify some large-scale NPP negative anomalies when there is no publication or report on them (Figure S6). We first filled data gaps caused by cloudiness in C5 16-day 1-km NDVI in a similar fashion to that applied to filling data gaps in 8-day FPAR/LAI (S*10*), then we calculated the growing season integrated NDVI using the above snow cover free period as growing season.

Text S3) Meteorological datasets

We used NCEP/DOE reanalysis II (S*7*) as the daily driving meteorological dataset for MODIS GPP/NPP. NCEP/DOE II is an improved version of the NCEP/NCAR reanalysis I model (S*16*) that fixed errors and updated parameterizations of physical processes (S*7*). The meteorological variables for MODIS GPP/NPP inputs, including daily minimum temperature (Tmin), daytime temperature (Tday), daily average temperature (Tavg), daily vapor pressure, and daily total downward short wave solar radiation (SWrad), were derived from 6-hourly NCEP/DOE II. At the global scale, though there are some biases in the surface variables of meteorological reanalysis datasets (S*14*, S*17*), NCEP/DOE II was found capable of capturing major changes in the surface climate anomalies (S*17*). We further verified the quality of temperature and downward solar radiation for the period from 2000 to 2009.

MODIS GPP/NPP algorithm uses daytime vapor pressure deficit (VPD) as water stress, and precipitation is not an input to the model (Equation 1). Though using VPD alone may fail to capture the seasonality of full water stresses over some regions with strong summer monsoon, it captures inter-annual variability of full water stresses and both seasonal and inter-annual variations of GPP when combining with remotely sensed FPAR since FPAR can partially reflect soil moisture stress (S*18*). For a thorough analysis, we used Palmer Drought Severity Index (PDSI) (S*19*) as a surrogate of soil moisture in warm seasons (S*20*) to independently measure changes in environmental water stress (Text S4).

Below details how we evaluated NCEP/DOE II datasets for the past decade.

1) Evaluation of surface air temperature from NCEP/DOE II

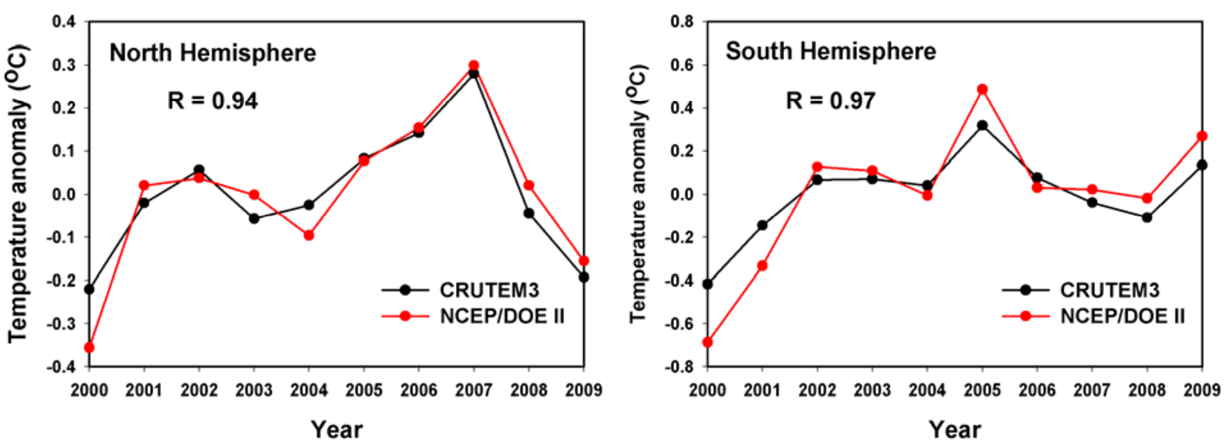

Figure S4. Comparison of the temperature anomalies from dataset CRUTEM3 with that from NCEP/DOE II from 2000 to 2009.

We compared air temperature of NCEP/DOE II with that from CRUTEM3 (S*21*), a global gridded temperature dataset based on instrumental measurements. Figure S4 shows the comparisons of inter-annual anomalies of surface air temperature over the two hemispheres on *vegetated* land areas from 2000 through 2009, demonstrating that surface temperatures from

NCEP/DOE II are reliable for our study. For both hemispheres, the correlations between the CRUTEM3 and NCEP/DOE II are significant (r >= 0.94, p < 0.0001).

2) Evaluation of solar radiation from NCEP/DOE II

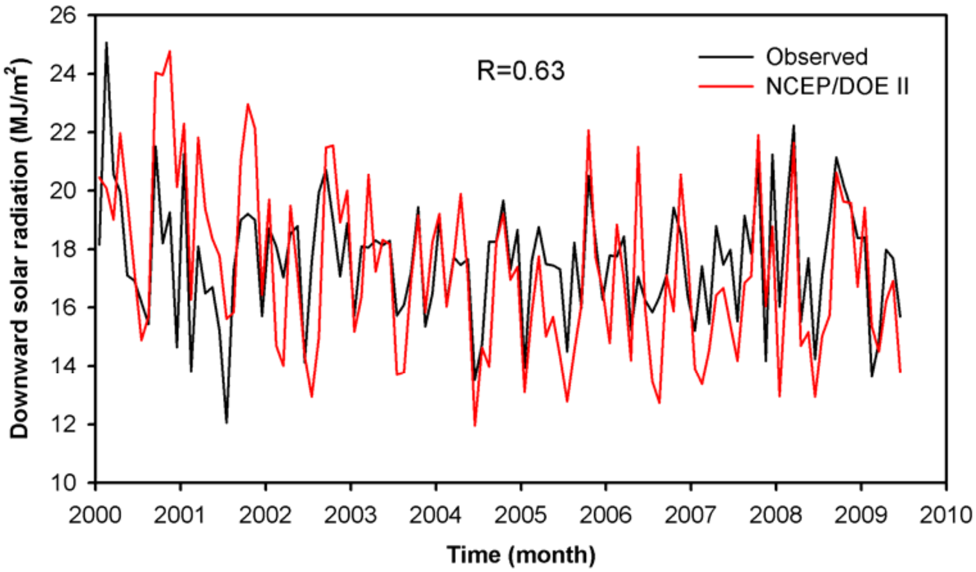

Figure S5. Comparison of monthly variation of mean downward solar radiation from the observed at a Baseline Surface Radiation Network (BSRN) site, MAN (full name: Momote, location is shown in Figure S9E), with that from NCEP/DOE II during the available observed data period January 2000 to June 2009 since 2000. Both shows decreased trends of SWrad from 2000 to 2009, with a linear trend $y= -0.0042 \cdot x + 17.811$ for the observed, and $y = -0.0303 \cdot x + 19.035$ for NCEP/DOE II.

Solar radiation generally contains larger uncertainties than surface air temperature in meteorological reanalyses (S*16*), and validation of solar radiation is challenging. Though remotely sensed cloudiness or SWrad can be used to compare with these from meteorological reanalyses, historical satellite data are found to contain artifacts mainly from shifts in view angle and satellite orbits and therefore to be inappropriate to be a reference for evaluation of reanalysis datasets (S*22*). Well-instrumented surface sites, such as Baseline Surface Radiation Network (BSRN), provide a reference to evaluate satellite retrievals and other data sources (S*22*). Here we used the 1 minute time interval measured downward global solar radiation from a station named Momote (short name MAN for BSRN stations), which is located in an island of Papua New Guinea (Latitude: -2.0580, Longitude: 147.4250, and Elevation: 6.0 m) (Figure S9E). The reason for choosing the station of MAN is that we are concerned about radiation changes in the humid rainforests, where solar radiation is the dominant control on vegetation growth (S*23*). There are only four BSRN stations located in or close to Amazon rainforests and Southeast Asian rainforests, and the short names are RLM, PTR, BRB and MAN (http://www.bsrn.awi.de/fileadmin/user_upload/Home/Maps/BSRN-Station-Global.png). However, from 2000 through 2009, there are only 2-month data in 2007 for RLM, 1-month in 2006 and 7-month in 2007 for PTR, 8-month in 2006 and 10-month in 2007 for BRB (http://www.pangaea.de/PHP/BSRN_Status.php?q=LR0100). Only the station of MAN has data from 2000 through June 2009. We aggregated minute measurements from MAN into monthly to evaluate the smoothed SWrad from four surrounding NCEP/DOE II cells (S*10*). Figure S5 shows monthly time series of SWrad from the measured and NCEP/DOE II. The correlation between the two is 0.63 ($n=114$, $p < 0.00001$), and both had decreased trends from 2000 to 2009, which is the underlying cause of the reduction of NPP in rainforests of Southeast Asia regions (Text S8). An increasing trend in precipitation over Southeast Asian rainforests may also imply more cloudiness and hence less solar radiation (Figure S9B, Figure S9E).

Text S4) Palmer Drought Severity Index (PDSI)

Among widely used drought indices (S*24*), PDSI (S*19*) is the only index which uses easily available monthly precipitation and temperature as input to assess drought (S*24*). It is impossible to devise a universal drought index because of the complexity of drought, and PDSI has limitations (S*24*). PDSI was originally designed to assess drought problems in semiarid climates, specifically, the Great Plains of the USA (S*19*), and thus some parameters may not work well for other regions (S*24*). Some assumptions in PDSI dealing with hydrological processes are also criticized, such as not treating frozen soil or snow accumulation and melt, and evapotranspiration occurring at the potential rate (S*20*, S*24*). Despite these limitations, Dai et al. (S*20*) found that PDSI correlates with soil moisture during warm seasons.

Palmer used a two-layer bucket model to quantify monthly water supply and demand by accounting for the input (precipitation), output (evaporation and runoff), and the antecedent soil water status. The model also considers multi-year average monthly water exchanges so that for a given month, the departure level of precipitation (supply) from the normal water demand can be quantified. Details of the Palmer model are described in S*19*.

However, the existing Dai et al.'s PDSI data (S*20*) only cover period through 2005, and the spatial resolution of 2.5 by 2.5 degree is not fine enough for our study. We calculated half degree global monthly PDSI for our study. Similarly to Dai et al. (S*20*), we use soil water holding capacity (*awc*) data from S*25*. If *awc* is no more than 2.54 cm (or 1 in.), then *awc* is assigned to the top soil layer, and the bottom layer has zero capacity, otherwise, the top layer has 2.54-cm water-holding capacity while the bottom layer has (*awc* - 2.54)-cm capacity. For monthly air temperature, we smoothed monthly mean surface air temperature from NCEP/DOE II into half-degree spatial resolution. For all precipitation data used in our study, we used monthly half-degree precipitation data generated by Chen et al (S*26*) based on gauge measurements at weather stations instead of that from NCEP/DOE II, since precipitation data from meteorological reanalysis datasets generally contain relatively large uncertainties (S*27*). We calculated half-degree PDSI from 1979 through 2009 but used PDSI from 2000 through 2009 to reduce the effects of initial status (i.e., spin-up effects). A lower PDSI generally implies a drier climate than a higher one.

Text S5) Contribution of global fire emissions to interannual CO_2 growth rate and of nitrogen deposition to NPP

Global fire emissions account for a substantial fraction of the variability of CO_2 growth rate (S*28*, S*29*). Based on the most recent estimated global fire carbon emissions over the period 1997-2009 (Table 7 in S*30*), the correlation between fire emissions and annual CO_2 growth rate (S*31*) is 0.65 ($p < 0.05$). For the period over 2000-2009, the correlation is still 0.65 ($p < 0.05$). This correlation, 0.65, is less strong than that between NPP and annual CO_2 growth rate either from a previous study, -0.71 ($p < 0.001$) (S*23*), or from this study, -0.89 ($p < 0.0006$), implying NPP is more strongly correlated with annual CO_2 growth rate than fire emissions. In the tropics and subtropics, most fires are set by humans for land clearing (S*32*). As climate regulates the amount of dry fuel available for ignition, it has a strong impact on the spatial and interannual variability of fire activity. In some regions, such as Indonesia, drought-induced biomass burning is amplified by the fires set by humans for deforestation and agricultural expansion (S*33*). The correlation between NPP and fire emissions is -0.55 ($p < 0.1$) from 2000 to 2009.

The impacts of nitrogen on the terrestrial carbon cycle are through three main mechanisms: enhanced photosynthesis, increased wood formation, and slowing soil decomposition (S*34*, S*35*). Since global nitrogen production and emissions continue to increase, and most nitrogen deposition occurs in the NH (S*36*), the increased NPP over the NH has some contributions from nitrogen fertilization, which may partially be reflected by the remotely sensed FPAR responding to enhanced canopy growth.

Text S6) Interannual variability of NPP

Table S2 lists websites for those large-scale droughts mentioned in the paper but with no particular refereed publication on them; Figure S7 shows the spatial pattern of yearly NPP anomalies for the past 10 years.

Table S2. Websites reporting large-scale droughts mentioned in the paper without relevant refereed publications for citations.

Region	Year	Webpage and Figure S6
China	2000	http://english.mep.gov.cn/SOE/soechina2000/english/climate/climate_e.htm
North America	2000	http://www.ncdc.noaa.gov/sotc/index.php?report=national&year=2000&month=ann
North America	2002	http://www.ncdc.noaa.gov/sotc/?report=drought&year=2002&month=13&submitted=Get+Report
Australia	2002	http://www.wwf.org.au/news/n36/
Africa	2005	Figure S6
Australia	2005	http://www.geo.uio.no/edc/downloads/the_australian_drought_of_2005_-_offprint_of_wmo_bulletin_2005_54%283%29_156-162.pdf
Australia	2007	http://www.bom.gov.au/climate/drought/archive/20090506.shtml
Australia	2008	http://www.bom.gov.au/climate/drought/archive/20090506.shtml
Australia	2009	http://www.bom.gov.au/climate/drought/archive/20090506.shtml

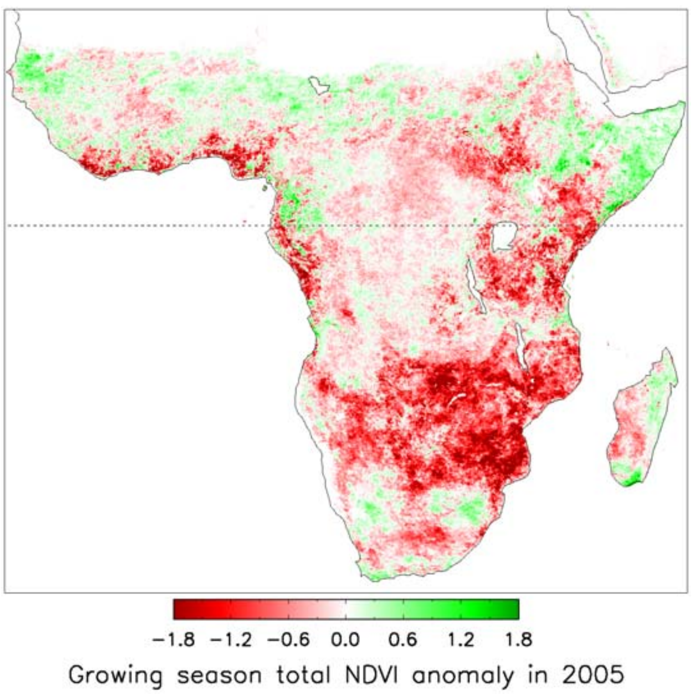

Figure S6. Negative anomaly of growing season total 16-day NDVI anomaly in 2005 over many parts of Africa supports 2005 drought over many parts of Africa as shown in Figure S7. We show NDVI anomaly because: 1) several reports on Internet about 2005 drought in Africa only mentioned East Africa, and 2) these reports were released in April 2005, not at the end of or after 2005, while anomaly of NPP in Figure S7 is annual.

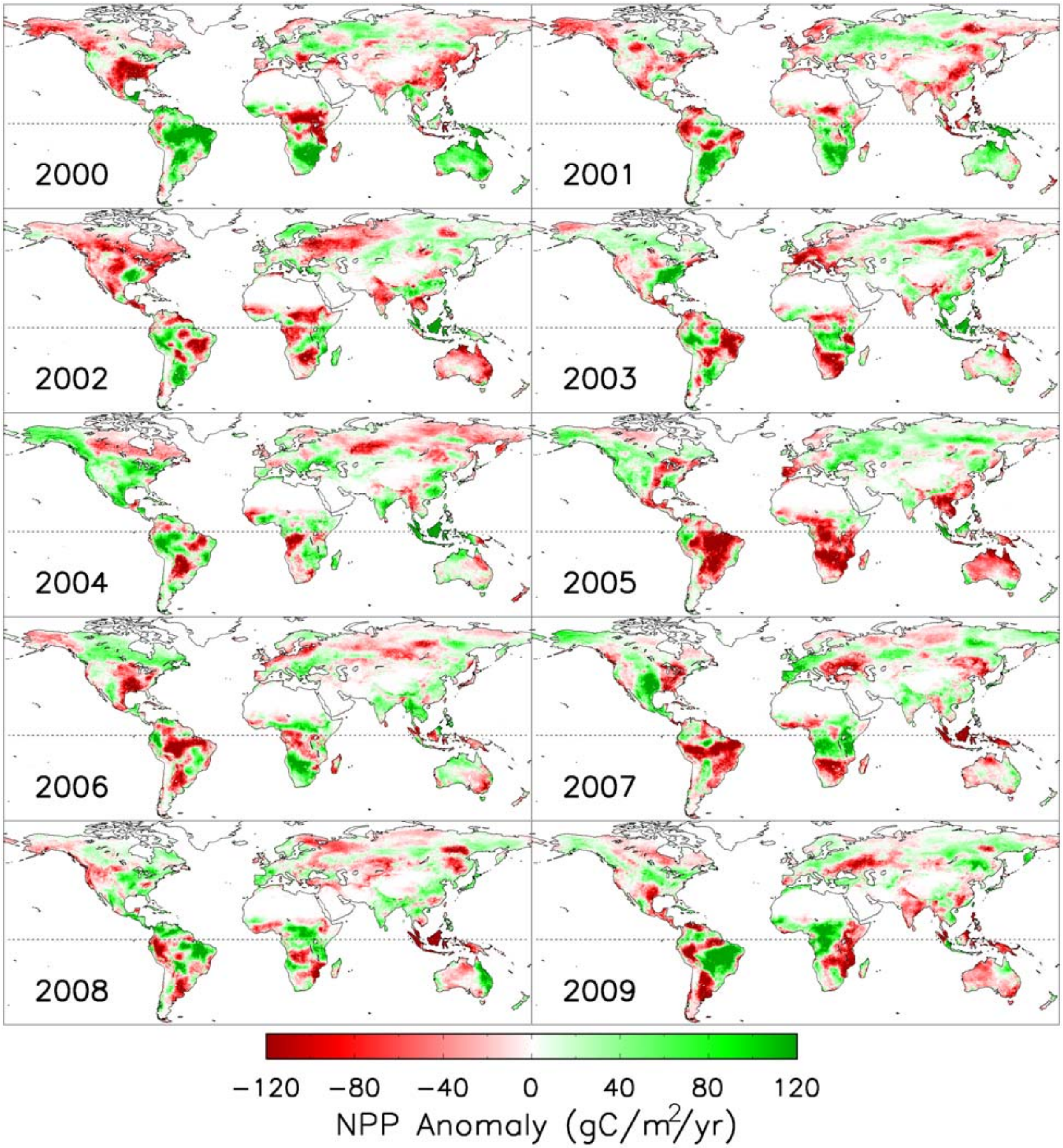

Figure S7. Spatial pattern of NPP variations from 2000 to 2009. Large-scale NPP negative anomalies were mainly caused by droughts. The reported droughts include: in 2000, droughts in large parts of North America, China; in 2002, drought in North America and Australia; in 2003, heat wave in Europe; in 2005, severe droughts in Amazon and drought in Africa and Australia; from 2007 to 2009, drought in Australia.

Text S7) Trends in NPP and climate variables and their relationships

Tables S3 summarizes the trends of NPP, Tavg, Precipitation (Prcp), SWrad, and PDSI, and the correlations between NPP and different climatic variables for major latitudinal zones, two hemispheres and the globe. Figure S8 through S10 show the spatial patterns of trends and changes of major climatic and remotely sensed variables, and the spatial correlations between NPP and major climatic variables.

Table S3. For the past decade (2000-2009), the linear trends of NPP, growing season air temperature (Tavg), precipitation (Prcp), downward solar radiation (SWrad), and Palmer Drought Severity Index (PDSI); and the correlations between NPP and these climatic variables for different latitudinal zones, over both hemispheres and the globe. All are area-weighted total or mean for vegetated land area only.

Latitudinal zones (% NPP in Globe)	NPP trend	Tavg trend Cor (NPP, Tavg)	Prcp trend Cor (NPP, SWrad)	SWrad trend Cor (NPP, SWrad)	PDSI trend Cor (NPP, PDSI)
47.5˚-90.0˚N (19.1)	*Y = 0.021·X-32.516*	*Y= 0.086 ·X -168.0009* *r = 0.55*	*Y= 0.147 ·X -12.34* *r = 0.38*	*Y= -0.648 ·X +4072.94* *r = -0.009*	*Y= -0.0135· X + 27.238* *r = 0.25*
22.5˚-47.5˚N (19.6)	*Y = 0.075·X-139.78*	*Y= 0.015·X -16.11855* *r = -0.07*	*Y= 3.781 ·X -6987.65* *r = 0.90****	*Y= 1.611·X + 2524.053* *r = -0.36*	*Y= 0.0895 · X - 180.15* *r = 0.76**
0.0˚-22.5˚N (19.9)	*Y = 0.031·X-52.146*	*Y= 0.0315·X -39.748* *r = -0.14*	*Y= 9.061 ·X -16781.23* *r = 0.31*	*Y= -21.99 ·X +50466.6* *r = -0.33*	*Y= 0.022 · X - 44.69* *r = 0.20*
North Hemisphere (58.6)	*Y = 0.128·X-224.44*	*Y= 0.048 ·X -84.218* *r = 0.48*	*Y= 3.604 ·X -6563.49* *r = 0.56*	*Y= -5.155 ·X +15021.8* *r = -0.84***	*Y= 0.031 · X - 62.13* *r = 0.39*
South Hemisphere (41.4)	*Y = -0.183·X+388.566*	*Y= 0.056 ·X -89.205* *r = -0.94****	*Y= 3.090 ·X -5028.45* *r = 0.50*	*Y= -0.458 ·X +7920.3* *r = -0.59*	*Y= -0.116 · X + 233.57* *r = 0.87***
Globe (100.0)	*Y = -0.055·X+164.124*	*Y= 0.050·X -85.73* *r = -0.64**	*Y= 3.448 ·X -6097.42* *r = 0.39*	*Y= -3.731 ·X +12868.3* *r = -0.32*	*Y= -0.014 · X + 27.81* *r = 0.48*

*: significant level of $p < 0.05$
**: significant level of $p < 0.01$
***: significant level of $p < 0.001$

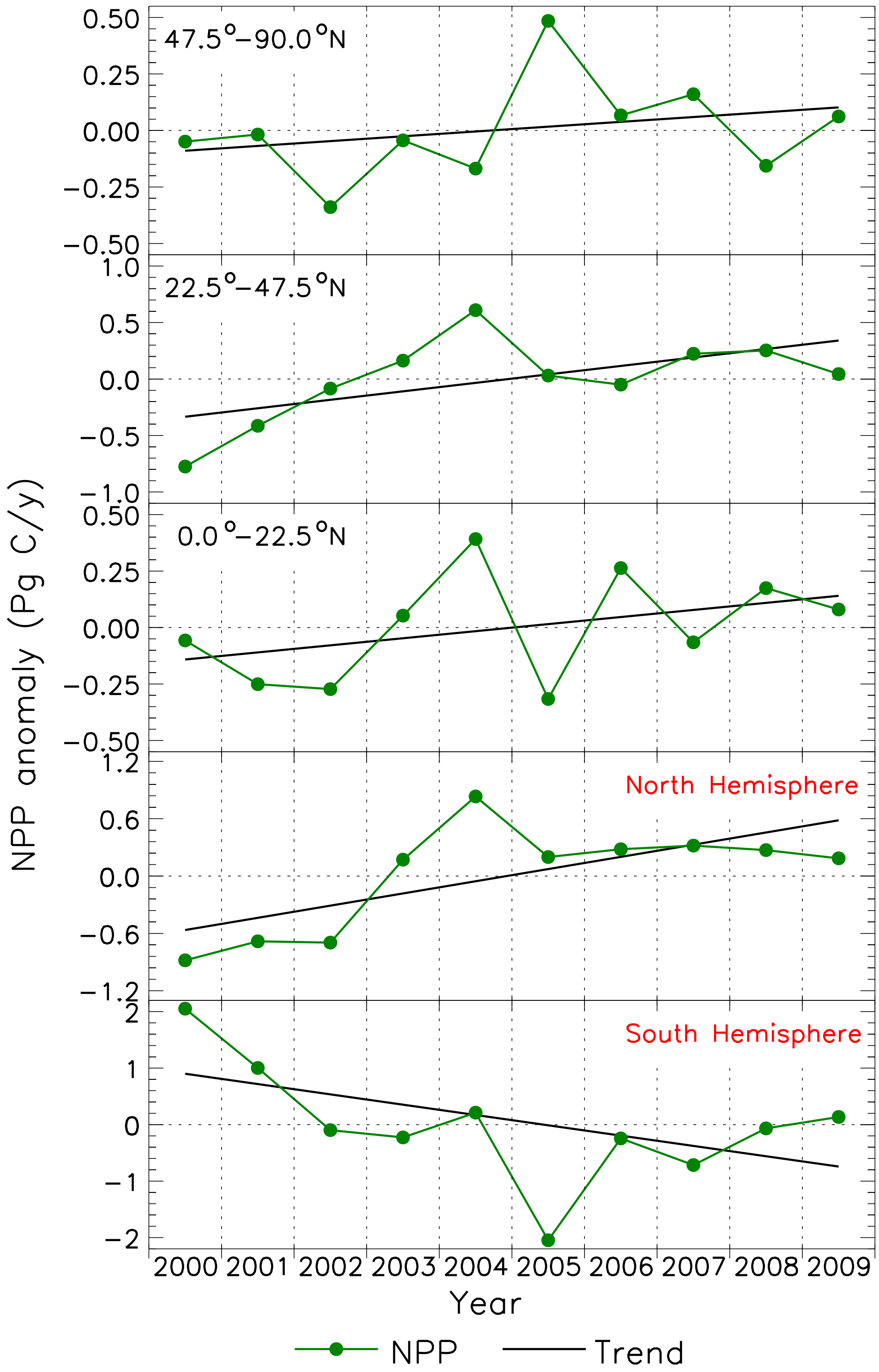

Figure S8. Annual total NPP variations and trends for different latitudinal zones and two hemispheres.

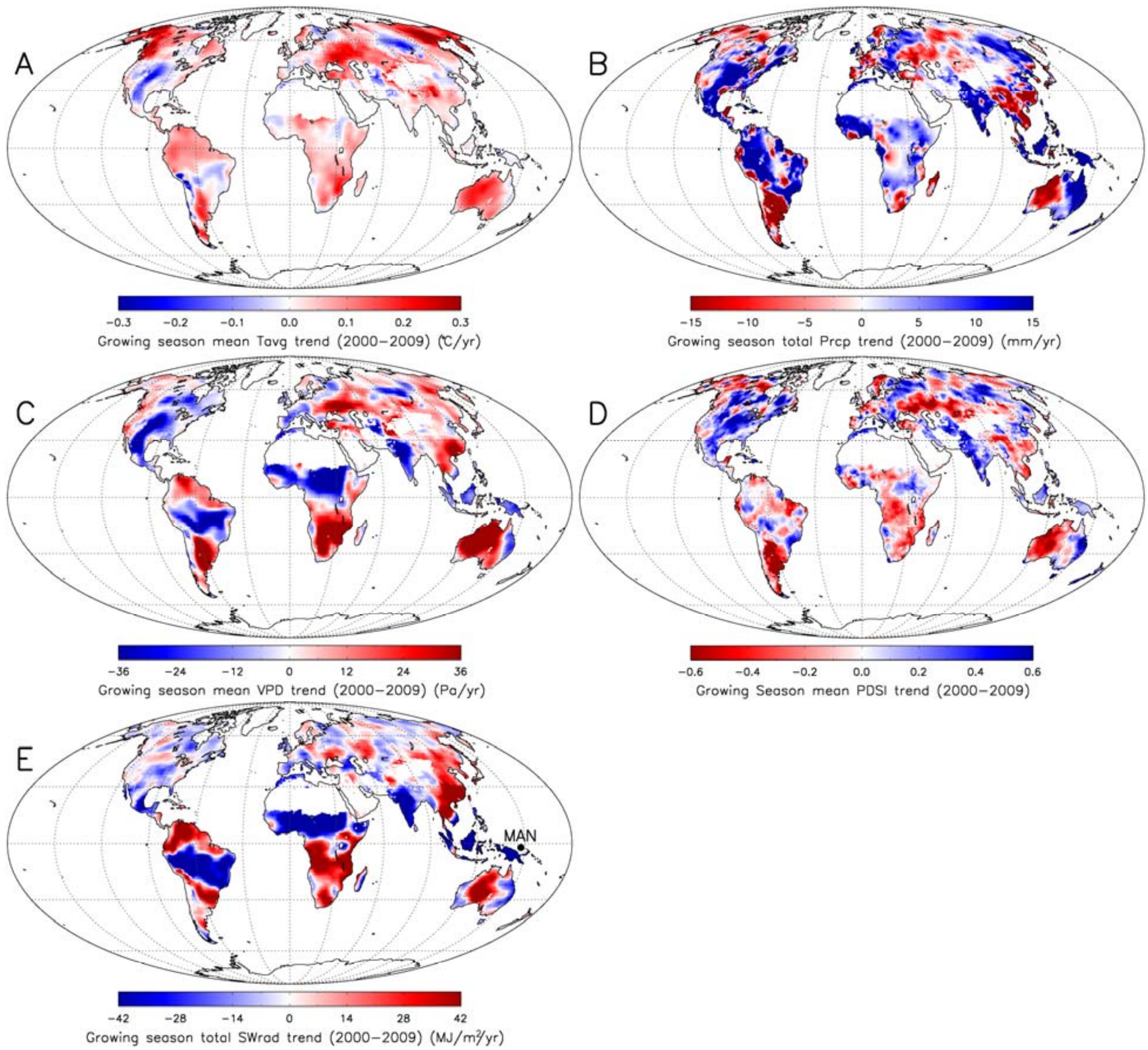

Figure S9. Spatial pattern of trends in annual growing season (A) average Tavg, (B) total Prcp, (C) average VPD, (D) average PDSI, and (E) total SWrad with the location of a BSRN station, MAN.

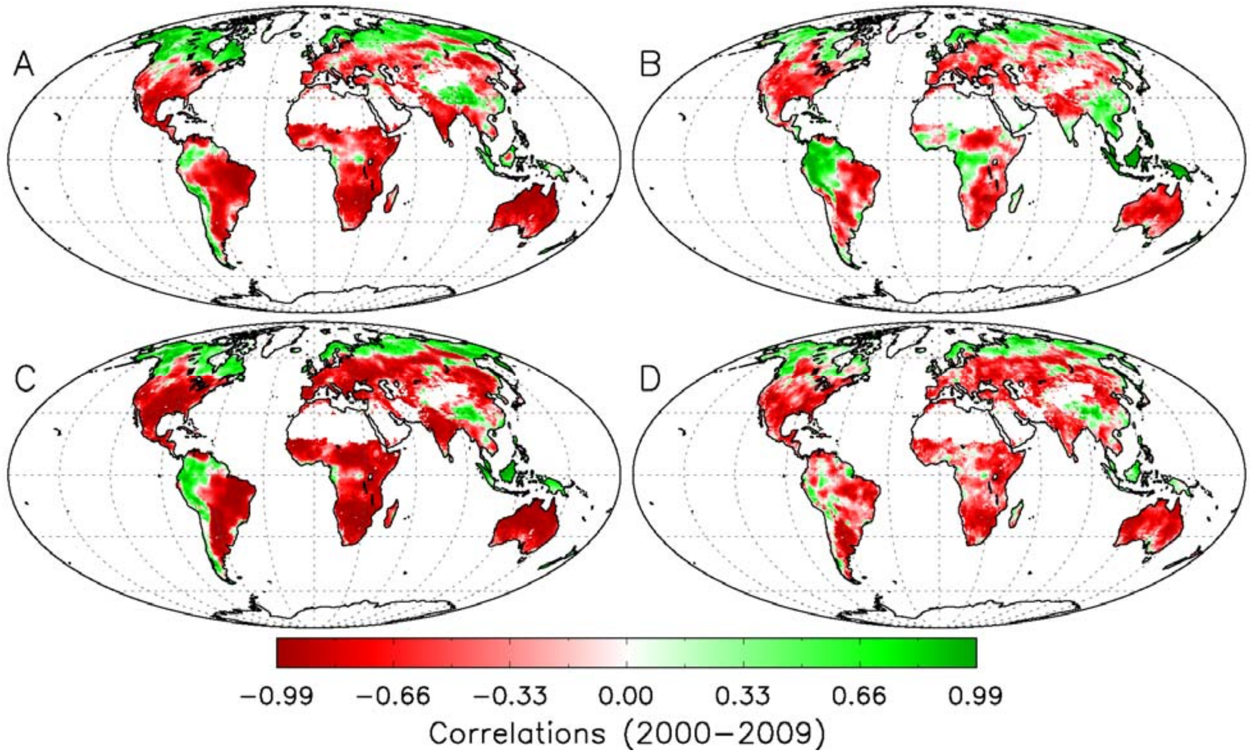

Figure S10. Spatial pattern of correlations between NPP and growing season (A) average Tavg, (B) total SWrad, (C) VPD, and (D) inverted PDSI.

Text S8) Detail study on tropical rainforests

Here we define tropical rainforests as Evergreen Broadleaf Forests (EBF) of MODIS land cover (Figure S2) within the area between the Tropic of Cancer and of Capricorn (23.5˚S-23.5˚N).

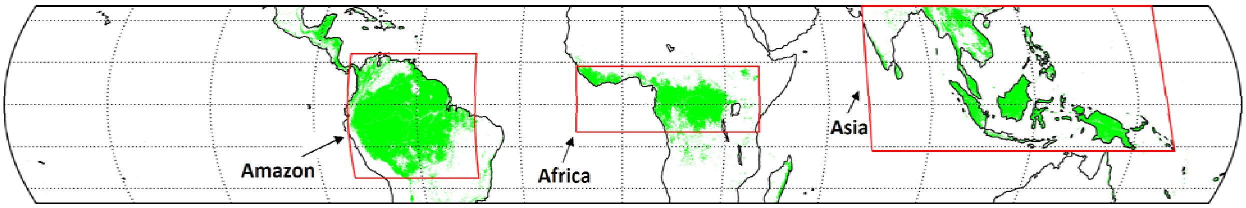

Figure S11. The spatial distribution of the tropical rainforests defined as evergreen broadleaf forests in MODIS land cover (Figure S2), and spatial ranges of the three major rainforests in Amazon, Africa and Asia. Rainforests are green colored.

Based on MODIS land cover data, there are 14.07 Million km^2 tropical rainforests, accounting for 13% of the global vegetated land. 10-year mean NPP for the tropical rainforests is 15.48 PgC/yr, accounting for about one third (28.92%) of the global total NPP (Table S4). To be more specific, the three major tropical rainforest regions are defined as: Amazon (17.5°S-12°N, 80°W-43°W), Africa (6.5°S-9°N, 13.5°W-40°E), and Asia (11°S- 23.5°N,73.5°E-162.5°E) (Figure S11).

Table S4. 10-year (2000-2009) NPP (PgC/yr) for the globe, tropics, tropical rainforests and three major regional tropical rainforests [Amazon, Africa and Asia (Figure S11)].

	2000	2001	2002	2003	2004	2005	2006	2007	2008	2009
Globe	54.692	53.841	52.727	53.465	54.565	51.672	53.557	53.123	53.725	53.841
Tropics	30.089	28.850	28.153	28.423	29.249	26.419	28.615	27.890	28.708	29.090
Tropical rainforests	16.207	15.525	15.677	15.808	15.963	14.625	15.138	14.915	15.319	15.608
Amazon rainforests	7.984	7.363	7.439	7.530	7.621	6.883	7.117	7.096	7.489	7.518
African rainforests	2.566	2.720	2.625	2.722	2.672	2.513	2.624	2.732	2.766	2.868
Asian rainforests	4.134	3.986	4.216	4.167	4.249	3.863	3.977	3.639	3.628	3.809

Based on Table S4, over the last 10-years, NPP in the tropics explains 93.0% ($r^2 = 0.93$, $p < 0.0001$) of interannual variations of the global NPP; Tropical rainforests explain 61.2% ($r^2 = 0.612$, $p < 0.008$) of interannual variations of the global NPP. For the three major rainforests, Amazon, Africa and Asia explain 65.5% ($r^2 = 0.655$, $p < 0.005$), 11.5% ($r^2 = 0.115$, $p < 0.5$) and 7.4% ($r^2 = 0.074$, $p < 0.5$) of the global NPP interannual variations, respectively, though NPP of Amazon accounts for 13.8% of the global NPP. Of the three major rainforests, only African

NPP had an increasing trend (0.189 PgC/10yr) mostly due to decreased VPD (Figure S9C), while the other two had decreasing trends with Amazon -0.424 PgC/10yr (Figure S12) and Asia -0.562 PgC/10yr.

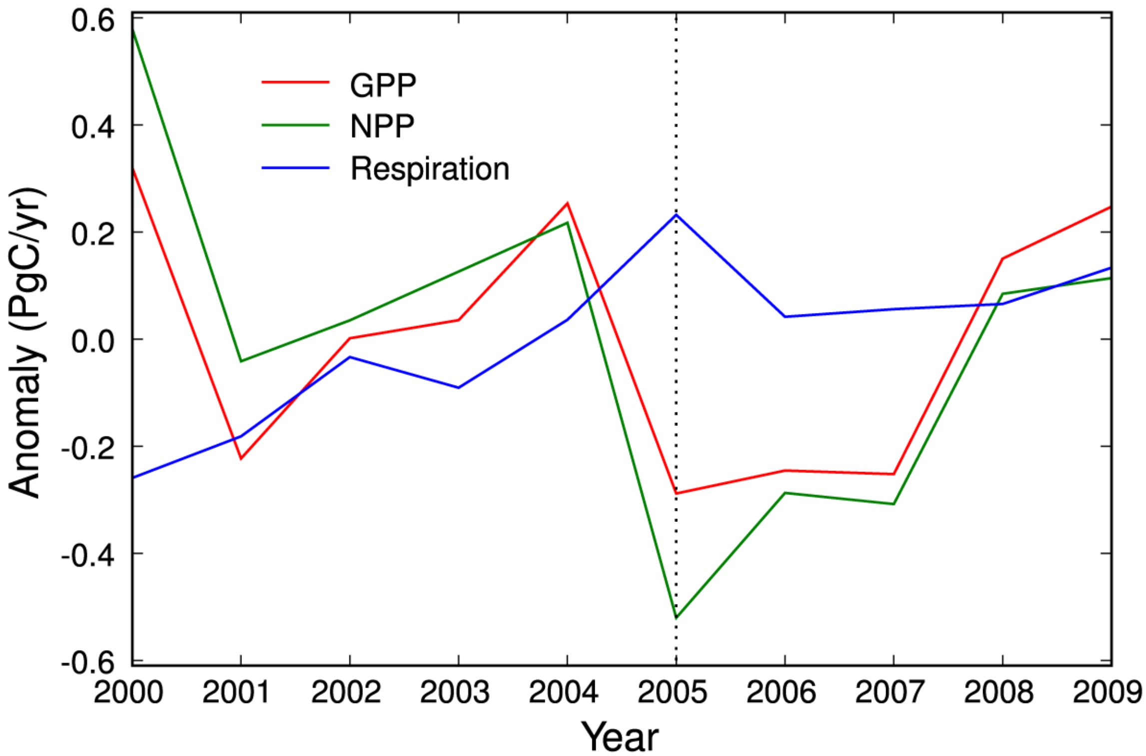

Figure S12. Inter-annual anomalies of GPP, NPP and autotrophic respiration of Amazon rainforests for the past decade with dotted line to denote 2005 drought.

Table S5. For the past decade (2000-2009), the linear trends of NPP, growing season air temperature (Tavg), precipitation (Prcp), downward solar radiation (SWrad), and Palmer Drought Severity Index (PDSI); and the correlations between NPP and other climatic variables for three major tropical rainforests [Amazon, Africa and Asia (Figure S11)]. All are area-weighted total or mean for vegetated land area only. The annual mean air temperature (˚C) and total precipitation (mm/yr) are also put in parentheses of the first column.

Rainforests (Tavg, Prcp)	NPP trend	Tavg trend Cor (NPP, Tavg)	Prcp trend Cor (NPP, SWrad)	SWrad trend Cor (NPP, SWrad)	PDSI trend Cor (NPP, PDSI)
Amazon (23.8, 2249)	*Y = -0.042·X+92.49*	*Y= 0.0703 ·X -117.096* *r = -0.79***	*Y= 12.844 ·X -23497.1* *r = -0.07*	*Y= -9.963 ·X +26047.55* *r = -0.27*	*Y= -0.02· X + 39.699* *r = 0.53*
Africa (23.9, 1678)	*Y = 0.019·X-35.21*	*Y= 0.029·X -34.823* *r = -0.06*	*Y= 3.348 ·X -5033.99* *r = 0.52*	*Y= 3.943·X -2125.172* *r = 0.09*	*Y= -0.086 · X + 171.25* *r = 0.43*
Asia (24.7, 2564)	*Y = -0.056·X+116.70*	*Y= 0.0003·X +24.01* *r = 0.20*	*Y= 15.92 ·X -29339.06* *r = -0.77***	*Y= -45.08 ·X +96432.8* *r = 0.95****	*Y= 0.041 · X – 81.43* *r = -0.41*

*: significant level of $p < 0.05$
**: significant level of $p < 0.01$
***: significant level of $p < 0.001$

Text S9) Amazon 2005 drought

Saleska et al (S*37*) reported that Amazon rainforests green-up during 2005 drought as there was higher Collection 4 (C4) EVI during dry season from July to September (JAS). Using EVI data in dry season of JAS can greatly reduce the issue of severe cloud contaminations in rainforests of the Amazon (S*37*). Samanta et al (S*38*) used the Collection 5 (C5) EVI and found there was no clear green-up in 2005. Here we examined changes of C5 FPAR/LAI, related climate variables, and resulting GPP and NPP changes in 2005 over Amazon rainforests. All the FPAR/LAI were cleaned to remove the cloud-contamination pixels (S*10*). Figure S13A shows spatial C5 FPAR changes in 2005 relative to the pre-2005 during JAS. Clearly, most areas exhibited "green-up". Though FPAR was higher in 2005, annual total NPP reduced (Figure S13B), which is largely consistent with many reductions of the rates of changes in the field measured above ground biomass (Figure S13C from Fig. 3C of S*39*). Note that for MODIS data, the pre-2005 is 2000 through 2004, while S*39* refers pre-2005 as 1998 through 2004.

To explore why higher FPAR in 2005 had a reduced NPP, we further examined the related variables. We did this at two temporal scales, one for the dry season (JAS) of the Amazon, and the other is for annual. We first calculated the standardized variable for each pixel (0.5 degree for climate variables and 1-km for other variables) over the last 10 years so that different variables can be comparable; then we got the area-weighted average of standardized variable over rainforests of the Amazon. Figure S14 shows area-weighted standardized variable of these variables over the last 10-years. During the dry season (JAS) of 2005, SWrad and VPD were the highest, while Prcp and PDSI were the lowest, implying that JAS in 2005 was the driest dry season for the past 10 years. Though in 2005, FPAR/LAI were the second highest during dry season, and the highest at yearly level in 2005, highest VPD induced lowest *fVPD*, greatly reducing GPP, and also the highest annual air temperature in 2005 induced the highest MRI and thus plant respiration (S*40*, S*41*). As a result, 2005 had the lowest NPP for the last 10-years in Amazon. Though it is unclear what caused higher FPAR/LAI in 2005, the general agreement of reduced NPP with the field data in 2005 reveals: 1) in some cases, remotely sensed greenness is not a proxy for NPP; 2) and remotely sensed NPP models require accounting for environment stresses and plant respiration.

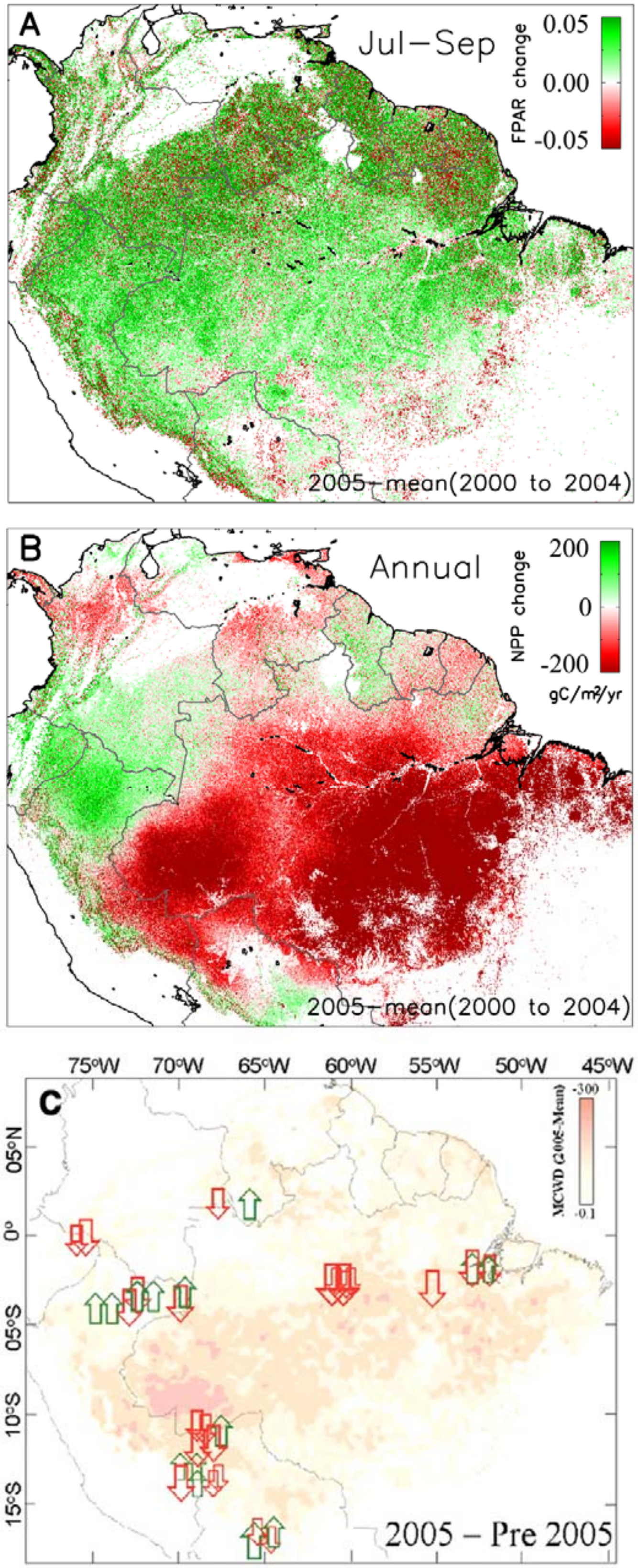

Figure S13. A) Collection 5 FPAR changes from July to September in 2005 relative to the period from 2000 through 2004; B) annual NPP changes relative the period from 2000 through 2004; and C) changes in the rates of above ground biomass relative to pre-2005 (1998-2004) (C is from Fig. 3C of S*39*). In A and B, results for pixels of rainforest (Figure S11) are only showed.

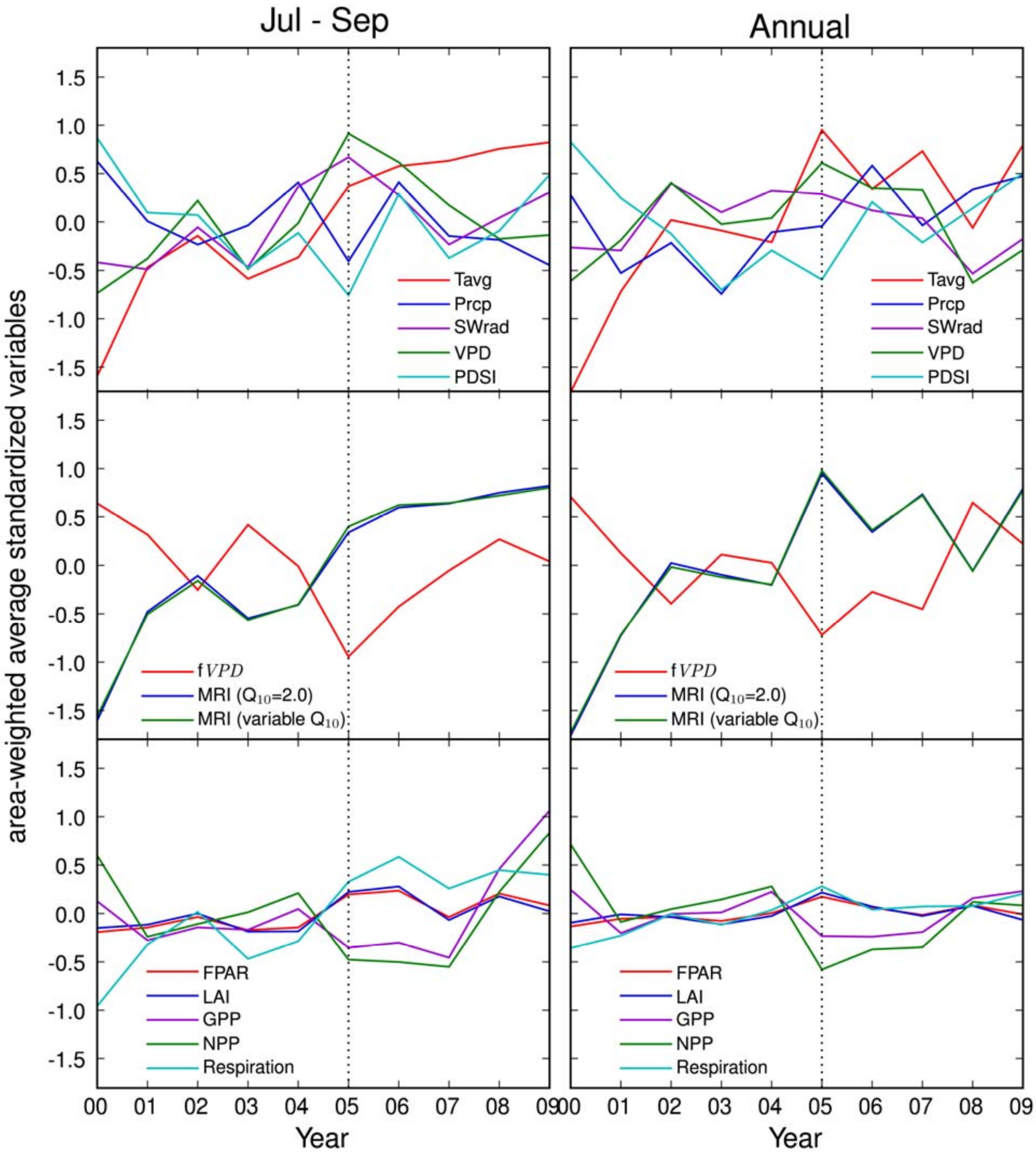

Figure S14. Area-weighted standardized variable for different climatic variables, derived biophysical variables, FPAR/LAI, GPP/NPP and autotrophic respiration for Amazon rainforests over the last decade. Left panel is for the dry season from July to September and right for the annual. Dotted vertical lines show drought of year 2005. The biophysical variables *fVPD* and MRI are defined in Equation 1, 4 and 5.

Text S10) Theoretical explanation on the sensitivity of water stress and plant maintenance respiration to different temperature levels

Saturation vapor pressure (SVP , in Pascal) is a function of air temperature (T , in Celsius) (S42),

$$SVP = 611 * \exp(\frac{17.502 * T}{T + 240.97}) \tag{6}$$

The derivation of SVP with respect to T is

$$\frac{dSVP}{dT} = SVP * \frac{17.502 * 240.97}{(240.97 + T)^2} \tag{7}$$

Maintenance respiration index (MRI) is a function of air temperature (T , in Celsius) (S3),

$$MRI = Q_{10}^{(\frac{T-20}{10})} \tag{8}$$

When Q_{10} is a constant value 2.0, it is applied to fine root and live wood components, and the derivation of MRI with respect to T is

$$\frac{dMRI}{dT} = MRI * \frac{\ln 2.0}{10} \tag{9}$$

When Q_{10} is not constant but a function of temperature (acclimation effect) for leaves (S5),

$$Q_{10} = 3.22 - 0.046 * T \tag{10}$$

the derivation of MRI with respect to T is

$$\frac{dMRI}{dT} = MRI * \left[\frac{0.046 * (20 - T)}{10 * (3.22 - 0.046 * T)} + \frac{\ln(3.22 - 0.046 * T)}{10} \right] \tag{11}$$

Table S6. Monthly and annual air temperature for vegetated land areas of the two hemispheres, North Hemisphere (NH) and South Hemisphere (SH).

	Jan	Feb	Mar	Apr	May	Jun	Jul	Aug	Sep	Oct	Nov	Dec	mean
NH	-1.412	0.048	4.329	9.523	14.437	18.390	20.363	19.283	15.585	9.976	4.031	-0.386	9.514
SH	24.439	24.068	23.168	21.528	19.157	17.556	17.327	19.035	21.333	23.076	23.816	24.264	21.564

Text S11) Calculation of temperature-limited vegetated area and their NPP

Figure S10A was used to calculate temperature-limited vegetated area and corresponding NPP. However, some positive correlations in the figure are not temperature-limited but solar radiation as there is a strong positive correlation between SWrad and temperature in many cases. To further rule out these non-temperature limited areas, we used average snow cover free days (Figure S3). The criteria for temperature limited area are these pixels with at least one month snow cover on average (32 days) and a positive correlation between NPP and temperature (Figure S10A). Based on the criteria, the temperature limited vegetated area is 26.5 Mkm^2, accounting for 24.3% of the global vegetated land area; the corresponding total average annual NPP is 8.6 PgC/yr, accounting for 16.1% global total NPP.

References and Notes

S1. S. W. Running, P. E. Thornton, R. R. Nemani, J. M. Glassy, in *Methods in Ecosystem Science*, O. Sala, R. Jackson, H. Mooney, Eds. (Springer-Verlag, New York, 2000), pp. 44–57.

S2. M. Zhao, S. Running, F. A. Heinsch, and R. Nemani, In *Land Remote Sensing and Global Environmental Change: NASA's Earth Observing System and the Science of ASTER and MODIS*. B. Ramachandran, C. Justice and M. Abrams, Eds (Springer-Verlag, New York 2010).

S3. M. G. Ryan, *Ecol. Appl.* **1**, 157 (1991).

S4. M. G. R. Cannell, J. H. M. Thornley, *Ann. Bot.* **85**, 45 (2000).

S5. M. G. Tjoelker, J. Oleksyn and P. Reich, *Glob. Change Biol.* **7**, 223 (2001).

S6. R. B. Myneni, *et al.*, *Remote Sens. Environ.* **83**, 214 (2002).

S7. M. Kanamitsu, *et al.*, *Bull. Amer. Meteor. Soc.* **83**, 1631 (2002).

S8. F. A. Heinsch, *et al.*, *IEEE Trans.Geosci. Remote Sens.* **44**, 1908 (2006).

S9. D. P. Turner, *et al.*, *Remote Sens. Environ.* **102**, 282 (2006).

S10. M. Zhao, F. A. Heinsch, R. R. Nemani, and S. W. Running, *Remote Sens. Environ.* **95**, 164 (2005).

S11. M. A. Friedl *et al.*, *Remote Sens. Environ.* **114**, 168 (2010).

S12. D. K., Hall, and G. A. Riggs, *Hydrol. Process.* **21**, 1534 (2007).

S13. A. Huete, *et al.*, *Remote Sens. Environ.* **83**, 195 (2002).

S14. M. Zhao, S. W. Running, and R. R. Nemani, *J. Geophys. Res.* **111**, G01002, doi:10.1029/2004JG000004 (2006).

S15. S. N. Goward, Tucker, C. J., & Dye, D. G., *Vegetatio* **64**, 3 (1985).

S16. E. Kalnay, *et al.*, *Bull. Amer. Meteor. Soc.* **77,** 437 (1996).

S17. A. K. Betts, *et al.*, *J. Geophys. Res.* **111**, D22S04, doi:10.1029/2006JD007174 (2006).

S18. Q. Mu, *et al.*, *J. Geophys. Res.* **112**, G01012, doi: 10.1029/2006JG000179 (2007).

S19. W. C. Palmer, *Research Paper 45, U.S. Dept. of Commerce* (1965).

S20. A. Dai, K. E. Trenberth, and T. Qian, *J. Hydrometeorol.* **5**, 1117 (2004).

S21. P. Brohan, J. J. Kennedy, I. Harris, S. F. B. Tett and P.D. Jones, *J. Geophys. Res.* **111**, D12106, doi:10.1029/2005JD006548 (2006).

S22. Norris, J. R. and A. Slingo, in *Clouds in the Perturbed Climate System: Their Relationship to Energy Balance, Atmospheric Dynamics, and Precipitation*. J. Heintzenberg and R. J. Charlson, Eds. (The MIT Press, 2009), pp. 17-36.

S23. R. R. Nemani, *et al.*, *Science* **300**, 1560 (2003).

S24. R. R. Heim Jr, *Bull. Amer. Meteor. Soc.* **83**, 1149 (2002).

S25. R. S. Webb, C. E. Rosenzweig, and E. R. Levine, *Glob. Biogeochem. Cycles*, **7**, 97 (1993).

S26. M. Chen, P. Xie, J. E. Janowiak, and P. A. Arkin, *J. Hydrometeorol.* **3**, 249 (2002).

S27. J. Chen, and M. G. Bosilovich, "Hydrological Variability and Trends in Global Reanalyses" (19th Conference on Climate Variability and Change, San Antonio, TX. January 2007).

S28. G. R. van der Werf, *et al.*, *Science* **303**, 73 (2004).

S29. G. R. van der Werf, *et al.*, *Atmos. Chem. Phys.* **6**, 3423 (2006).

S30. G. R. van der Werf, *et al.*, *Atmos. Chem. Phys. Discuss.* **10**, 16153 (2010).

S31. Global CO_2 annual growth rate is available at http://www.esrl.noaa.gov/gmd/ccgg/trends/

S32. G. R. van der Werf, J. T. Randerson, L. Giglio, N. Gobron, A. J. Dolman, *Global Biogeochem. Cycles* **22**, GB3028, doi:10.1029/2007GB003122 (2008).
S33. R. D. Field, G. R. van derWerf and S. S. P. Shen, *Nat. Geosci.* **2**, 185 (2009).
S34. F. Magnani, *et al.*, *Nature* **447**, 848 (2007).
S35. I. A. Janssens, *et al.*, *Nat. Geosci.* **3**, 315 (2008).
S36. D. S. Reay, F. Dentener, P. Smith, J. Grace, and R. A. Feely, *Nat. Geosci.* **1**, 430 (2008).
S37. S. R. Saleska, K. Didan, A. R. Huete, H. R. da Rocha, *Science* **318**, 612 (2007).
S38. A. Samanta, *et al.*, *Geophys. Res. Lett.* **37**, L05401, doi:10.1029/2009GL042154 (2010).
S39. O. L. Phillips, *et al.*, *Science* **323**, 1344 (2009).
S40. D. A. Clark, S. C. Piper, C. D. Keeling, and D. B. Clark, *Proc. Natl. Acad. Sci. USA* **100**, 5852 (2003).
S41. Y. Malhi, *et al.*, *Glob. Change Biol.* **15**, 1255 (2009).
S42. A. L. Buck, *J. Appl. Meteorol.* **20**, 1527 (1981).